Applied Surface Science Advances 34 (2026) 100999

Contents lists available at ScienceDirect

Applied Surface Science Advances

journal homepage: www.sciencedirect.com/journal/applied-surface-science-advances

Photoelectrochemical performance and charge dynamics of supersonic cluster beam deposited $CuFe_2O_4$ thin films

Michele Vergari [a], Skerxho Osmani [a], Ermanno Pierobon [b], Enrico Scattolin [b], Andrea Basagni [b], Alberto Gasparotto [b,c], Chiara Maurizio [d], Gian Andrea Rizzi [b,c,**], Luca Gavioli [a,*]

[a] Interdisciplinary Laboratories for Advanced Materials Physics (i-LAMP) & Dipartimento di Matematica e Fisica, Università Cattolica del Sacro Cuore, Via della Garzetta 46, 25131 Brescia, Italy
[b] Department of Chemical Sciences, Padova University, Via Marzolo 1, 35131 Padova, Italy
[c] CNR-ICMATE and INSTM, Department of Chemical Sciences, Padova University, Via Marzolo 1, 35131 Padova, Italy
[d] Department of Physiscs and Astronomy, Padova University, Via Marzolo 8, 35131 Padova, Italy

ARTICLE INFO

Keywords:
Copper ferrite films
Photocathode
IMPS, SCBD, HER

ABSTRACT

Developing efficient and stable photoelectrodes is a major challenge in photoelectrochemical energy conversion technologies. Although $CuFe_2O_4$ is a promising p-type semiconductor, its implementation as a photocathode has been limited by the difficulty of synthesizing uniform and stable films and by the scarce investigation of its charge-transfer kinetics. In this work, a 70 nm thick $CuFe_2O_4$ layer was fabricated for the first time by supersonic cluster beam deposition, enabling the direct growth of a homogeneous and nanogranular film on a FTO substrate. After air annealing at 400 °C, compositional and structural characterizations revealed the formation of a polycrystalline tetragonal spinel-type $CuFe_2O_4$ film, with a Cu_xO segregation at the surface. Despite its low thickness, the electrode displayed strong visible light absorption and a p-type photoelectrochemical activity in neutral electrolyte (0.1 M Na_2SO_4), with a good electrochemical stability. Interestingly, below 0.4 V *vs.* RHE applied bias, the charge injection kinetic constant drop corresponds to the reduction of Cu^{2+} surface species to Cu^{+}. The absorbed photon to current conversion efficiency spectra revealed a peak efficiency at 2.8 eV and confirmed a bias-dependent feature associated with the Cu_xO interfacial layer.

1. Introduction

Harnessing solar energy through photoelectrochemical (PEC) processes demands systems that combine stability, efficiency, and elemental abundance. Copper ferrite ($CuFe_2O_4$), a spinel-type ternary oxide [1] composed of earth-abundant elements, has emerged as a viable photocathode material for solar-driven hydrogen production [2], CO_2 [3,4] and nitrates reduction [5]. Its moderate band gap (1.6–2.8 eV), high chemical stability, and visible-light absorption, make it particularly suitable for integration into PEC cells [6].

Since $CuFe_2O_4$ is a highly promising material, several synthesis routes have been explored, each presenting specific drawbacks in terms of processing complexity, thermal requirements, or film quality. Standard solid-state routes require high calcination temperatures (600900 °C [7]), whereas chemical methods, such as sol-gel combustion [8] and electrospinning [9] might require long reaction times and often yields powders rather than uniform films [4,10] complicating their integration into PEC devices. Furthermore, wet-chemical routes depend on auxiliary reagents that necessitate post-synthesis washing and may introduce residual impurities [4,10], often requiring also a final calcination step [7–9].

It is also essential understanding the $CuFe_2O_4$ interfacial charge transfer kinetics, since its PEC performances are often limited by surface recombination and inefficient charge injection into the electrolyte. Intensity modulated photocurrent spectroscopy (IMPS) provides critical insights into the dynamic response of photocathodes under modulated illumination [11,12]. By probing the frequency-dependent photocurrent behaviour, IMPS enables separation of bulk charge transport kinetics from surface charge transfer processes. This technique has already been used to investigate $CuFe_2O_4$ behaviour as photoanode [13,14], however

* Corresponding author.
** Corresponding author at: Department of Chemical Sciences, Padova University, Via Marzolo 1, 35131 Padova, Italy.
E-mail addresses: gianandrea.rizzi@unipd.it (G.A. Rizzi), luca.gavioli@unicatt.it (L. Gavioli).

https://doi.org/10.1016/j.apsadv.2026.100999
Received 15 December 2025; Received in revised form 9 April 2026; Accepted 30 April 2026
Available online 5 May 2026

reports regarding its implementation as photocathode are missing.

In this work, $CuFe_2O_4$ thin films were prepared using a pulsed microplasma cluster source coupled with a supersonic cluster beam deposition (PMCS-SCBD, hereafter SCBD for the sake of clarity) apparatus, a method that allows direct fabrication of homogeneous and nanostructured films with tuneable morphology and stoichiometry [15–18]. In addition, SCBD does not involve chemical precursors, ensuring that no extrinsic contaminants are introduced during deposition.

A deep structural, chemical, morphological and optical characterization revealed that, upon air annealing at a temperature as low as 400 °C, 70±8 nm thick polycrystalline $CuFe_2O_4$ films with a Cu_xO ultrathin surface layer are formed, showing a strong visible-light absorption. PEC measurements, carried out in a neutral and non-corrosive electrolyte (0.1 M Na_2SO_4), unlike most reports relying on highly concentrated alkaline solutions [2,19,20], revealed promising photocurrent densities of 0.1 mA/cm^2 at 0.35 V *vs.* RHE. These values are comparable to the best performances reported in neutral electrolytes [2], yet with a film thickness much lower than those typically reported in the literature (hundreds of nanometres or microns) [19,20].

Under chopped visible-light illumination, the photocurrent decreased by just 20 % in more than two hours, a substantial improvement over the hundreds of seconds stability windows commonly reported [2,20]. The IMPS analysis provided the bias dependent charge kinetic constants and revealed the role of the Cu_xO surface layer on charge injection into the electrolyte. Overall, the present results provide novel fundamental insight on the behaviour of $CuFe_2O_4$ photoelectrodes and a possible efficient route for their synthesis.

2. Experimental procedures

2.1. Synthesis

A supersonic beam of nanoparticles (NPs) is generated via 50 bar helium plasma spark ablation of a $CuFe_2$ metal rod, see **Figure S1** of the Supplementary Material (SM). A synchronized 750 V pulse is applied to the rod at 3 Hz frequency, generating a NPs-gas mixture that is extracted from the ablation chamber through a nozzle. The beam is subsequently focused by a set of aerodynamic lenses, and a skimmer is used to select its central section to reduce NPs size distribution. The NPs are simultaneously deposited at 10^{-6} mbar directly on FTO-coated glass (Sigma Aldrich, FTO thickness = 550 nm; surface resistivity ≈7Ω/square; glass thickness = 2 mm) and on single crystalline Si(111) substrates (Siltronix, thickness 0.5 mm). The electrodes are obtained directly by exposing substrates to the NPs beam while monitoring in real time the film thickness by a quartz microbalance. The samples deposited on FTO were subsequently annealed at 400 °C in air for two hours and used for the structural, optical, compositional and electrochemical characterization, while Si–supported samples were used to measure film thickness by atomic force microscopy (AFM).

2.2. Physical characterization

X-ray diffraction (XRD) measurements were performed in a glancing incidence mode (ϑ_i = 1.0°) using a Bruker AXS D8 Advance Plus diffractometer, equipped with a Göbel mirror and a CuK_α X-ray source (λ = 1.54051 Å). Patterns were collected in the 15–65° 2θ range with a step size of 0.06° and an acquisition time of 5 s/step.

Raman spectra were collected with a Renishaw-Invia system, equipped with a 532 nm laser source and an 1800 lines/mm grating. The laser with an 8 mW power was focused onto the sample with a 100 × objective.

The morphology and microstructure of the samples were characterized by transmission electron microscopy (TEM) and high-angle annular dark-field scanning transmission electron microscopy (HAADF-STEM) using a TEM JEOL F200 instrument operated at 200 kV. Elemental analysis and mapping were performed using a JEOL 100 mm^2 silicon drift energy dispersive X-ray (EDX) spectrometer. Samples for TEM observation were prepared scratching out the deposits from the FTO substrate, mixing with ethanol and depositing the obtained suspension on carbon-supported gold grids (400 mesh size).

AFM data (2 × 2 μm^2 area at 1024 × 1024 pixels) were acquired with a Park NX10 instrument, operating in noncontact mode employing PPP-NCHR tips (NanoAndMore GMBH) for $CuFe_2O_4$ layers onto FTO. The images were processed with Gwyddion software. The film roughness was determined as the root mean square (RMS) deviation of the pixel height distribution. The deposited film thickness (d) was measured on the Si(111) substrate by 10 × 2 μm^2 images on scratched areas. Kelvin probe force microscopy (KPFM) measurements were performed with the same instrument employing PPP-CONTSC Pt tips to acquire the work function (φ) of the film onto FTO. A −2.4 V sample bias and a 1.9 V drive voltage were applied. The tip used was calibrated by setting, in the same operating condition, the HOPG work function at 4.6 eV. The calibration has been checked measuring a φ of 5.05 eV for a 35 nm thick Au film.

Scanning electron microscopy (SEM) analysis was performed with a Zeiss Sigma HD microscope, equipped with a Schottky FEG source, one detector for backscattered electrons and two detectors for secondary electrons (InLens and Everhart Thornley). A low acceleration voltage of 5 kV was used in order to accurately delineate fine surface features. The microscope is coupled to an EDX detector (from Oxford Instruments, x-act PentaFET Precision) for X-rays microanalysis, working in energy dispersive mode. All the spectroscopic measurements were performed at 10 kV. The AZtec software (from Oxford Instruments) was used to collect and process X-ray spectra.

Film composition was investigated by X-ray photoemission spectroscopy (XPS) using a non-monochromatic Mg X-ray source (incident photon energy 1253.6 eV) and a Phoibos 100 SPECS analyzer at 20 eV pass energy. Data were acquired with 0.1 eV/step for the $CuFe_2O_4$ electrodes deposited onto FTO substrates. The data were analyzed using CasaXPS software and XPST Igor plugin. Due to the presence of overlapping signals from Auger lines, intense satellite structures, and the enhanced inelastic scattering contribution arising from the intrinsic porosity of the films, we adopted an active background approach, following ref [21]. The background, constituted by combined Shirley, linear, and Tougaard contributions, was included in the fitting procedure and optimized together with the peak parameters to preserve physically meaningful constraints, such as literature branching ratios and spin–orbit splitting values. The peak components were fitted using a Gaussian–Lorentzian product function with a GL(50) lineshape. During the fitting procedure, the spin–orbit doublet was constrained by fixing the area ratio to 0.51, consistent with the expected branching ratio [22,23]. All spectra were corrected for charging by assigning a binding energy (BE) of 284.8 eV to the main component of C 1 s peak.

Optical data were acquired in 250–2500 nm range with a Perkin-Elmer Lambda950 spectrophotometer equipped with an integrating sphere. The optical absorption coefficient (α) was calculated from transmittance (T) and specular reflectance (R) spectra, using the following relation to account also for multiple internal reflections [24,25]:

$$\alpha(h\nu) = \frac{1}{d} ln\left[\frac{(1-R)^2}{2T} + \sqrt{\frac{(1-R)^4}{4T^2} + R^2}\right] \quad (1)$$

where $h\nu$ is the incident photon energy. The T, R and absorbance (A) spectra for the bare FTO substrate are reported in **Figure S2** of the SM.

2.3. PEC characterization

Photoelectrocatalytic activity tests were performed at room temperature by an integrated system consisting of a Zennium-PRO and a PP212 unit from Zahner GmbH, coupled with an optical bench equipped

with a Zahner photoelectrochemical cell. A Pt wire and a standard Ag/AgCl electrode [$V_0 = 0.21$ V *vs.* reference hydrogen electrode (RHE)] were used as counter and reference electrodes respectively, whereas the FTO-supported $CuFe_2O_4$ sample was used as working electrode. The electrical contact was made by sticking a stripe of copper tape on the edge of FTO conductive face.

Linear sweep voltammetry (LSV) measurements were performed in a N_2-deaerated Na_2SO_4 0.1 M aqueous solution (pH = 6) using a scan rate of 5 mV/s. The light source was a AM 1.5 solar simulator (incident power = 100 mW/cm^2). IMPS analyses were carried out applying a LED frequency between 5000 and 1 Hz with a 15 % of light intensity modulation. The white light intensity was set at 50 mW/cm^2. Electrochemical impedance spectroscopy (EIS) data were acquired from 100 mHz to 10 kHz with a 5 mV potential modulation.

Mott-Schottky (MS) plots were obtained recording EIS spectra between 0.50 to 0.26 V *vs.* RHE, with 0.05 V steps. Capacitance of the semiconductor (C_{sc}) was obtained from the EIS spectra fitted with a R(RQ) circuit shown in **Figure S3** of SM, while the flat band potential (V_{FB}) was obtained by fitting the linear part of the $1/C_{sc}^2$ *vs.* potential plot and finding the intercept with the voltage axis, using the equation [26,27]:

$$\frac{1}{C_{sc}^2} = \frac{2}{(\varepsilon_0 \varepsilon_r e N_D)}\left(V - V_{FB} - \frac{k_B T}{e}\right) \quad (2)$$

where ε_0 is the permittivity of free space, ε_r the relative permittivity of the target material, e the electron charge, N_D the concentration of majority charge carriers, k_B the Boltzmann constant, and T the absolute temperature. In this model, it was assumed that the Helmholtz capacitance C_H is >> C_{SC} and so the total capacitance C is ~ C_{sc}, since C_H and C_{sc} are in series with each other.

The incident photon-to-current conversion efficiency (IPCE) is a measure of the ratio of the photocurrent (converted to an electron transfer rate) *vs.* the rate of incident photons (converted from the calibrated power of a light source) as a function of wavelength [28]. The IPCE (%) considers the efficiencies for photon absorption/charge excitation and separation ($\eta_{e/h}$), charge transport within the solid to the solid–liquid interface (η_{tr}), and interfacial charge transfer across the solid–liquid interface (η_{CT}). The IPCE was measured in the potential interval 0.6 to 0.35 V *vs.* RHE, and the values were calculated as follows:

$$IPCE(\%) = \frac{(1240 \times j)}{(P \times \lambda)} \times 100 \quad (3)$$

where j is the photocurrent density (mA/cm^2), λ is the incident light wavelength (nm), and P is the incident light power density for each wavelength (mW/cm^2). Measurements were obtained by using fourteen different LED light sources with wavelengths between 365 and 810 nm. The LEDs wavelength separation is ranging from 20 to 65 nm (from 0.06 to 0.33 eV) see **Table S1**. Each source light intensity was measured in real time by a photodiode during LSV acquisition. The absorbed photon to current conversion efficiency (APCE) was calculated from the absorbance A = 1-R-T using the following equation [29]:

$$APCE(\%) = \frac{IPCE}{A} \quad (4)$$

3. Results and discussion

3.1. Structural and chemical characterization

Fig. 1a shows a representative 2 × 2 μm^2 AFM image of sparse NPs on Si(111) surface before the annealing. CuFe NPs are the bright spots

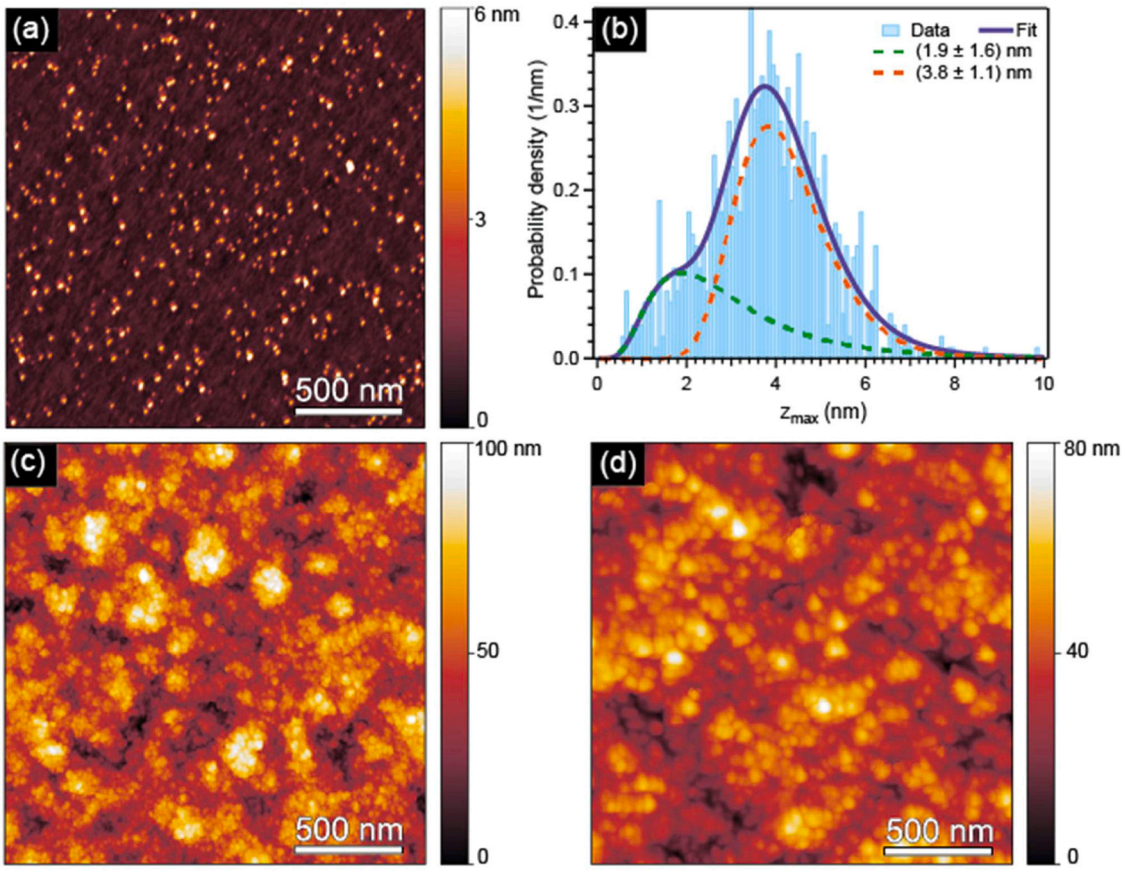

Fig. 1. (a) 2 × 2 μm^2 AFM images of sparse CuFe NPs (bright spots) deposited on Si(111) surface, (b) CuFe NPs height distribution. 2 × 2 μm^2 AFM images of 65 nm CuFe NPs layer on FTO substrate before (c) and after (d) the annealing.

emerging from the dark substrate. The NPs height (z_{max}) was extracted from several AFM images. The height, unlike the in-plane dimensions, is unaffected by tip convolution effects and reliably reflects NPs size. The height distribution (blue bars) of NPs obtained from a set of 910 values is reported in Fig. 1b. The fit (purple curve) reveals a double lognormal distribution, with the first peak (green dashed curve) centred at 1.9 ± 1.6 nm and the latter (red dashed curve) at 3.8 ± 1.1 nm. A multimodal lognormal distribution of the NPs size is typical of the SCBD deposition method, in particular when NPs composed of multiple elements are obtained [16,30–32].

Fig. 1c reports a 2 × 2 μm^2 AFM image of the film deposited on FTO before the thermal treatment. As reported in **Figure S4** of the SM, the film exhibits an estimated thickness of 65±6 nm. An average RMS roughness of 14 nm was measured, comparable to the one of the bare FTO substrate, suggesting a conformal growth and a homogeneous coating. NPs assemble into larger aggregates consistently with the ballistic aggregation growth process [33], but the presence of distinct individual NPs remains evident in Fig. 1c.

Fig. 1d instead reports a 2 × 2 μm^2 AFM acquisition after the annealing step in air. Individual as-deposited NPs can no longer be distinguished, as they have merged into larger nanostructures. This coalescence phenomenon leads to a smoother surface, with the RMS roughness decreasing to 11 nm. For the same specimen, cross-sectional SEM imaging evidenced a well-adherent deposit with a uniform thickness of 70±8 nm (**Figure S5**). According to EDX analysis, the film featured a Fe/Cu overall ratio of 2.0 ± 0.2, in good agreement with TEM results (see below).

The XRD pattern (red curve) of the FTO-supported annealed sample is reported in Fig. 2a. As can be observed, besides reflections due to the substrate marked with symbol * (for comparison, XRD spectrum of a bare FTO substrate is also displayed (black curve)), two additional peaks at 2ϑ = 35.5 and 43.3° can be discerned, attributed respectively to the (211) and (220) crystallographic planes of the $CuFe_2O_4$ tetragonal spinel phase (space group I41/amd, PDF 00-34-0425). The average crystallite size, estimated through the Scherrer equation, turned out to be 15±3 nm.

Fig. 2b shows the Raman spectra acquired under 532 nm excitation in the 190–800 cm^{-1} range. The peaks at 219, 286, 337, 450, 520, 633 and 685 cm^{-1} match the vibrational fingerprints expected for tetragonal $CuFe_2O_4$ [34,35]. In particular, the strong A_{1g} stretching modes over 600 cm^{-1} are fully consistent with the distortions induced by the Jahn-Teller active Cu^{2+} ions in octahedral sites, which stabilize the tetragonal phase [34].

In this regard, important complementary insights were provided by TEM analyses. A fragment of the film is shown in Fig. 3a. The selected area electron diffraction (SAED) pattern reported in Fig. 3b is consistent with the tetragonal $CuFe_2O_4$ phase, as the main diffraction rings expected from reference card PDF 00-034-0425 can be identified. Specifically, the measured interplanar spacings can be assigned to (112), (103)/(211), (202), (220), (312), (105)/(303), and (321) family of planes. The pattern exhibits diffuse yet complete Debye rings, indicating a polycrystalline material with small crystallite size, together with a few isolated bright spots, typically associated with the presence of some larger crystallites.

High-resolution TEM (HR-TEM) images further confirm the polycrystalline nature of the material (see **Figure S6** in SM). Several overlapping crystallites can be observed, while isolated grains are only occasionally visible. The average size, estimated over 21 crystallites, is 8.1 nm, in good agreement with the value of 15 nm obtained from X-ray diffraction, considering that the XRD signal tends to be dominated by larger crystals.

Although the SAED pattern reveals the predominance of the $CuFe_2O_4$ phase, the local compositional analysis performed by STEM-EDX indicates a non-uniform distribution of the constituent metals, as can be observed in Fig. 3c. In particular, the average Cu:Fe atomic ratio over the entire aggregate is 1:1.77, suggesting a slight copper excess compared to the expected stoichiometric ratio of 1:2. In some regions of the sample (Fig. 4a), a gradual variation of the Cu:Fe ratio can be observed, ranging from the stoichiometric 1:2 value in the more homogeneous areas to Cu-enriched zones with ratios up to 81:1. HR-TEM images collected from these Cu-rich regions reveal crystallites with interplanar spacings of 0.26 nm and 0.18 nm, consistent with the presence of the CuO phase (PDF 01-080-0076; Fig. 4b and c). These observations, combined with the XPS analysis below, indicate that, while $CuFe_2O_4$ is the dominant phase, a partial CuO formation occurs within the film, possibly resulting from non-uniform metal distribution during the thermal treatment.

Fig. 5 compares the Cu 2p and Fe 2p XPS and the Cu LMM Auger

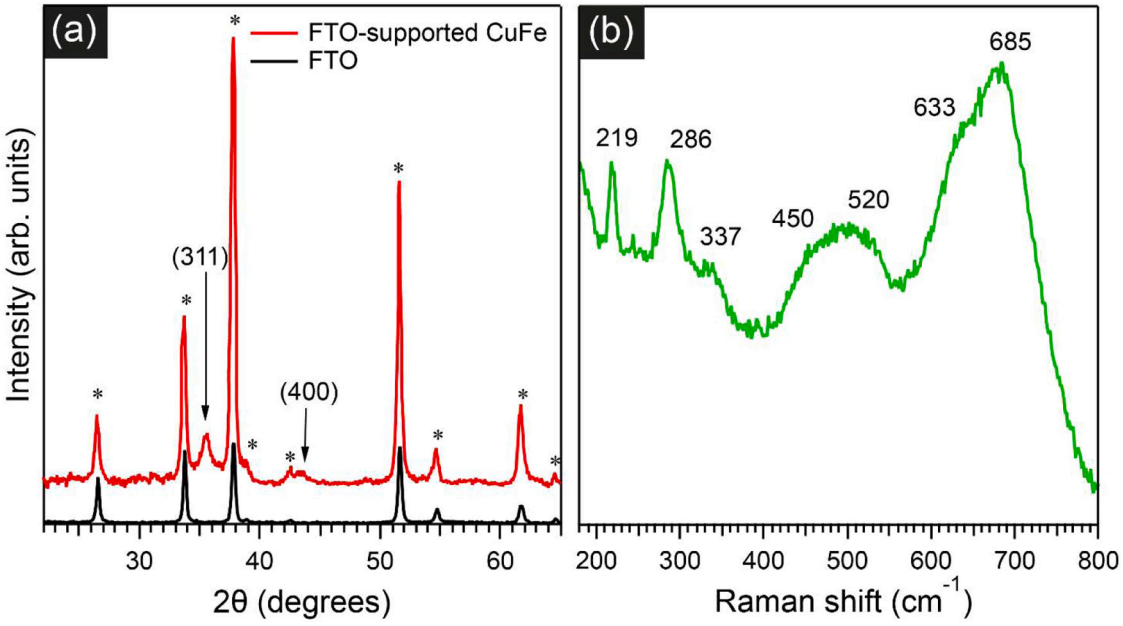

Fig. 2. XRD (a) and Raman (b) spectra of FTO-supported CuFe layer after thermal treatment in air at 400 °C (red and green spectra respectively). For comparison, the XRD spectrum of a bare FTO substrate is also displayed (black curve).

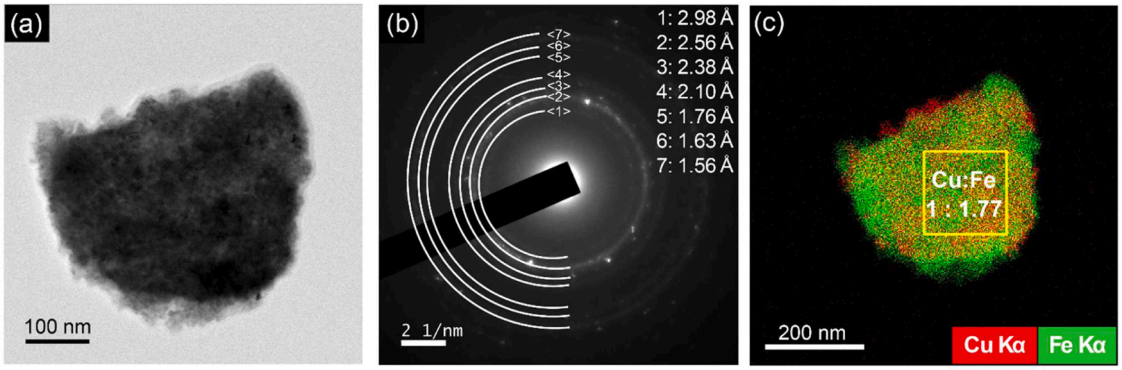

Fig. 3. (a) Low-magnification bright-field TEM image of the $CuFe_2O_4$ sample. (b) Corresponding SAED pattern, in which the white semicircles highlight the experimental diffraction rings. The measured interplanar spacings are consistent with the tetragonal $CuFe_2O_4$ phase, as reported in PDF 00-034-0425. (c) STEM–EDX elemental map showing the spatial distribution of copper and iron within the aggregate. The average Cu:Fe atomic ratio is also indicated.

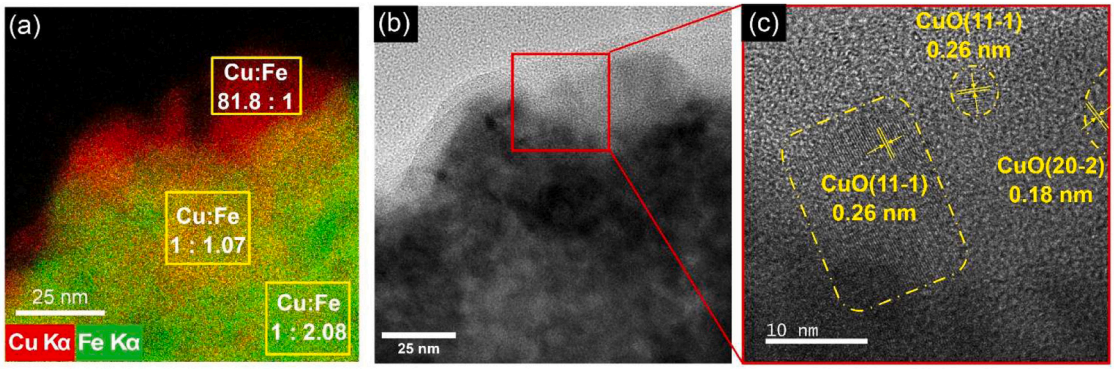

Fig. 4. (a) STEM-EDX elemental mapping illustrating the presence of a Cu rich area. The Cu:Fe atomic ratio calculated in the area highlighted in yellow is also reported. (b) Bright-field TEM image of the same area analyzed in (a); (c) HR-TEM image of the copper rich area.

spectra for the FTO-supported electrodes before and after annealing. The details of the deconvolution results for the XPS spectra, including the O1s and C1s signals (displayed in **Figure S7**), are reported in **Table S2** and **S3**.

Fig. 5a shows the Cu 2p spectrum before the thermal treatment, together with the peak deconvolution performed according to the work of Torres et al [22]. The two components reproducing the $2p_{3/2}$ peak (blue curves) may be attributed to contribution from both Cu^0 and Cu^+[22]. Since the Cu^0 and Cu^+ binding energies are too close to be distinguished [22], the presence of both species becomes evident from the Auger spectrum shown in Fig. 5b. The $L_3M_{45}M_{45}$ Auger transition exhibits two distinct peaks as already observed for copper alloys exposed to air [36]: one at 918.6 eV kinetic energy, attributed to the metallic Cu [22,23] and another at 916.1 eV attributable to the Cu^+oxidation state [37]. The Cu^+ presence can be attributed both to the deposition method, as trace amounts of oxygen may be present in the chamber where the plasma is generated, and to air exposure during the sample transfer to the XPS chamber.

After the thermal treatment the presence of shake-up satellites in the Cu 2p spectrum (Fig. 5d) suggests the appearance of a Cu^{2+} oxidation state [22]. However, the intensity ratio between the satellite features and the main peak of this state rules out a complete oxidation of the sample to Cu^{2+}. The Cu^{2+} contribution as deduced from the green curve deconvolution is 54 % of the Cu 2p signal, while the Cu^+ peak (blue curve) accounts for the 46 % of the signal. The Cu($L_3M_{45}M_{45}$) Auger lineshape reported in Fig. 5e is centred at 917.6 eV in agreement with the presence of CuO [23].

Fig. 5c reports the Fe 2p spectrum before annealing. Due to the presence of the O(KLL) Auger transition peaked at 742 eV [38], an additional artificial component (light grey curve) was included in the fit to account for its contribution. Therefore, given the complexity of the background, the XPS quantification is affected by relatively large uncertainty margins. Switching to the Al Kα excitation worsens this issue, as the Fe 2p region then overlaps with the Cu $L_3M_{23}M_{23}$ Auger emission [39]. According to the literature peak assignment [40], the Fe 2p spectrum shows no evidence of metallic Fe before the thermal treatment, but only Fe^{2+} and Fe^{3+} components (orange and blue curves, respectively) with a relative ratio Fe^{2+}:Fe^{3+} of ~1:2.

The annealing results in a substantial decrease of the surface Fe signal, further compromised by the presence of the O(KLL) Auger transition as shown in Fig. 5f. The Fe 2p is dominated by the Fe^{3+} component [41] although, due to the high noise level and the complex background, a minor contribution of Fe^{2+} cannot be completely excluded. A decrease in iron content is clearly reflected in the Cu:Fe ratio, which shifts from 1:2.8 in the as-deposited film to 30:1 upon annealing. It should be noted that the decrease in iron content refers only to the near-surface region probed by XPS. This observation, consistent with the TEM and STEM-EDX results, suggests the formation of a Cu_xO-rich region at the surface during thermal treatment, as already observed in other studies [6].

The optical absorption in semiconductors can be described by the relation:

$$\alpha^n = B(h\nu - E_g) \quad (5)$$

where B is a proportionality constant and E_g represents the band gap energy [25]. The exponent n depends on the nature of the electronic transition, taking a value of 1/2 for indirect transitions and 2 for direct transitions.

Fig. 6a displays the experimental data (orange dots) employing eq. 5

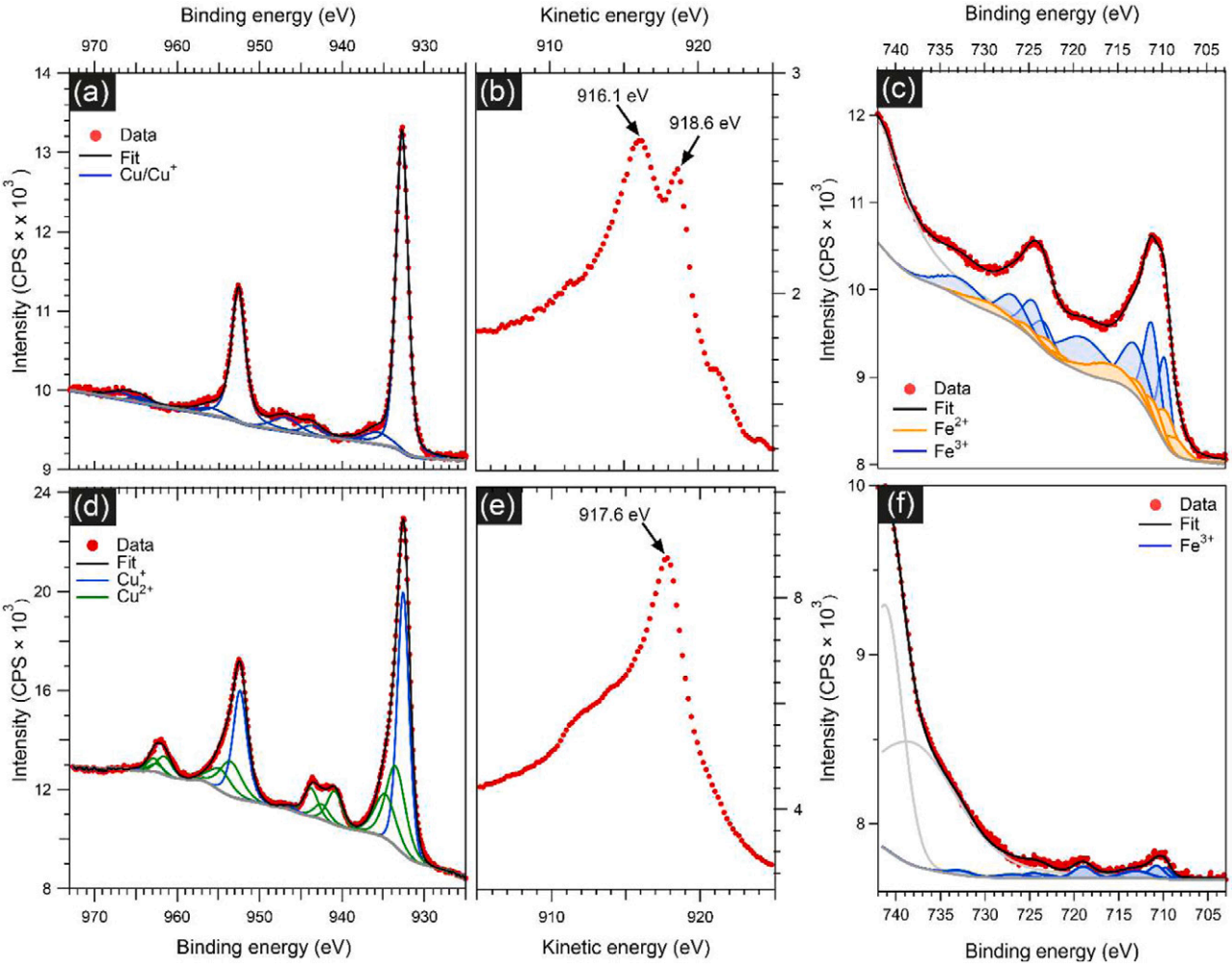

Fig. 5. XPS spectra (red dots) of the CuFe layer on FTO substrate as deposited [(a-c)] and after annealing [(d-f)]. The black line represents the fitted results after background subtraction (grey line). Deconvoluted components are also shown. Panels (a) and (d) display the Cu 2p spectra, with Cu^0/Cu^+ (blue) and Cu^{2+} (green) contributions. The corresponding Cu Auger $L_3M_{45}M_{45}$ spectra are reported in panels (b) and (e). Panels (c) and (f) report the Fe 2p spectra, with Fe^{2+} (orange) and Fe^{3+} (blue) peaks. For Fe 2p the fitting was obtained by considering the multiplet splitting of Fe^{3+} and Fe^{2+} signals.

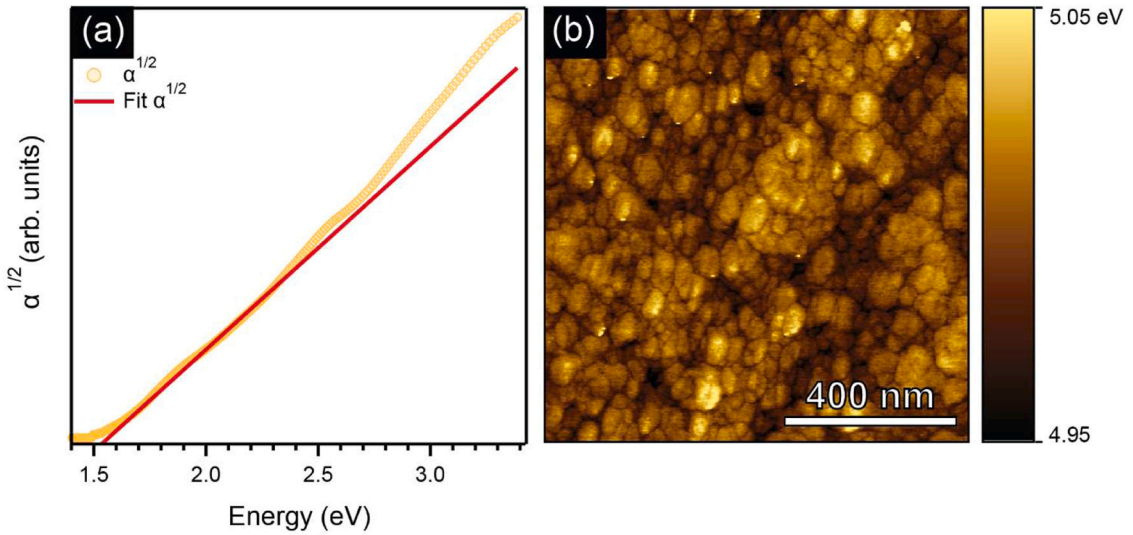

Fig. 6. (a) Experimental data (orange dots) plotted as $\alpha^{1/2}$ *vs*. the photon energy in the 1.4–3.8 eV range. The red solid line represents the linear fit to extract E_g value. (b) 1 × 1 μm^2 KPFM image representing the work function of CuFe film.

with the $\alpha^{1/2}$ *vs.* $h\nu$ scale. The linear fit (red curve) suggests that the indirect band gap is 1.55 ± 0.1 eV, in good agreement with literature values for $CuFe_2O_4$ [42,43]. Determining the direct band gap is on the other hand challenging, due to the extended Urbach tail [44]. As detailed in the SM section 8 (**Figure S9**), the α^2 fit yields a value of 2.8 ± 0.2 eV.

Fig. 6b shows the work function (φ) map obtained through KPFM on a 1 × 1 μm^2 film region. The mean φ value is approximately 5 eV with respect to the vacuum level. This value falls within the 4.5–5.2 eV range reported for $CuFe_2O_4$ films deposited by other methods [14,45]. Notably, the narrow spread of the local φ values suggests a limited degree of electronic inhomogeneity across the probed area, indicating uniform grain composition and a well-defined surface stoichiometry.

3.2. Photoelectrochemical characterization of $CuFe_2O_4$ electrodes

The $CuFe_2O_4$ electrode demonstrates promising PEC properties, as illustrated in Fig. 7a. LSV scans under chopped light (green curve), in the dark (blue curve), and under continuous illumination (red curve) were recorded in a 0.1 M Na_2SO_4 solution, previously deaerated with nitrogen for 20 min. A constant nitrogen flow was maintained throughout the measurements. The yellow curve in the same figure represents the photocurrent obtained under identical conditions but illuminating the sample by a solar simulator with an intensity of 100 mW/cm^2. As expected, the photocurrent density nearly doubles, indicating that the electrode operates in a photon-limited regime with no significant injection or recombination bottlenecks under the experimental conditions.

The electrode exhibits p-type behaviour, with a photocurrent onset for the HER at approximately 0.6 V *vs.* RHE, indicating efficient photoactivity. This onset potential aligns with values reported by other researchers [2,46,47] (see **Table S4** in SM for a comparison of PEC performances of Cu-based ferrites reported in the literature). The dark current remains stable up to 0.4 V *vs.* RHE, beyond which a slight increase suggests a reduction process, likely involving the CuO at the surface, which is reduced to Cu_2O [48]. This behaviour is also observed in the chopped chronoamperometry, where the dark current slightly shifts up from −0.006 to −0.004 mA/cm^2 over the scan duration (Fig. 7b). Despite this, the electrode maintains good stability during two hours of continuous PEC operation, with only a 20 % decrease in photocurrent, underscoring its reliability and performance.

Fig. 8a presents the MS plot for the $CuFe_2O_4$ electrode in a nitrogen-deaerated 0.1 M Na_2SO_4 solution. The negative slope of $1/C^2$ confirms the expected p-type behaviour. The flat band potential (V_{FB}) is approximately 0.5 V *vs.* RHE (4.95 V *vs.* Vacuum), and in line with the KPFM measurements of Fig. 6b. We attribute the higher position of V_{FB} if compared with values reported in the literature to the presence of Cu^+ surface species (see XPS results above) [2,49]. Notably, the high constant values of $1/C^2$ at potentials above V_{FB} correspond to a rather low double-layer capacitance, suggesting a relatively flat film morphology (see AFM data in Fig. 1).

These findings, combined with the optical band gaps derived from Tauc plots (Fig. 6), support a proposed junction scheme involving a thin CuO/Cu_2O overlayer surrounding $CuFe_2O_4$ particles. This junction is known to have a positive effect on the photocurrent density [47]. Depending on the position of the CuO valence band edge [2,50], either a Z-scheme or a type II junction may form (Fig. 8b). In the latter case, electron injection occurs into CuO crystallites, whereas in the Z-scheme, the electrolyte directly contacts the $CuFe_2O_4$ surface.

Fig. 9a displays normalized IMPS Nyquist plots recorded at increasing bias potentials in 0.1 M Na_2SO_4. These plots enable rapid extraction of pseudo-kinetic constants: the injection rate constant (k_{inj}) and the recombination rate constant (k_{rec}) [11,51]. Key features include the high-frequency intercept (HFI) on the right, the low-frequency intercept (LFI) on the left, and the peak frequency (ω_{max}). These parameters allow calculation of kinetic constants using the following relations:

$$\omega = k_{inj} + k_{rec} \tag{6}$$

$$\eta_{inj} = \frac{LFI}{HFI} = \frac{k_{inj}}{k_{inj} + k_{rec}} \tag{7}$$

The Nyquist plots in Fig. 9a reflect charge transfer processes at low frequencies from the photoactive surface to the electrolyte. Moving from higher potential (V = 0.53 V) towards lower values (V = 0.38 V), *i.e.*, towards a cathodic regime, the analysis shows that k_{inj} increases (red squares) while k_{rec} decreases (green dots) as shown in Fig. 9b. This is consistent with the progressive increase of the photocurrent intensity, due to the charge transfer from the photocathode towards the solution, during HER. It is interesting to note that a sharp drop in k_{inj} occurs when the potential is decreased below 0.4 V *vs.* RHE, coinciding with Cu_2O formation, which has unfavourable band edge positions and impairs injection kinetics (Fig. 9c) [50]. At the same time, this strongly suggests that the photocurrent measured in the range of higher potential values (0.4–0.6 V) arises from HER and ORR, and not from CuO reduction. Indeed, if Cu_2O formation begins as the photocurrent develops (0.6 V), no increase in k_{inj} should be observed with decreasing bias. Moreover,

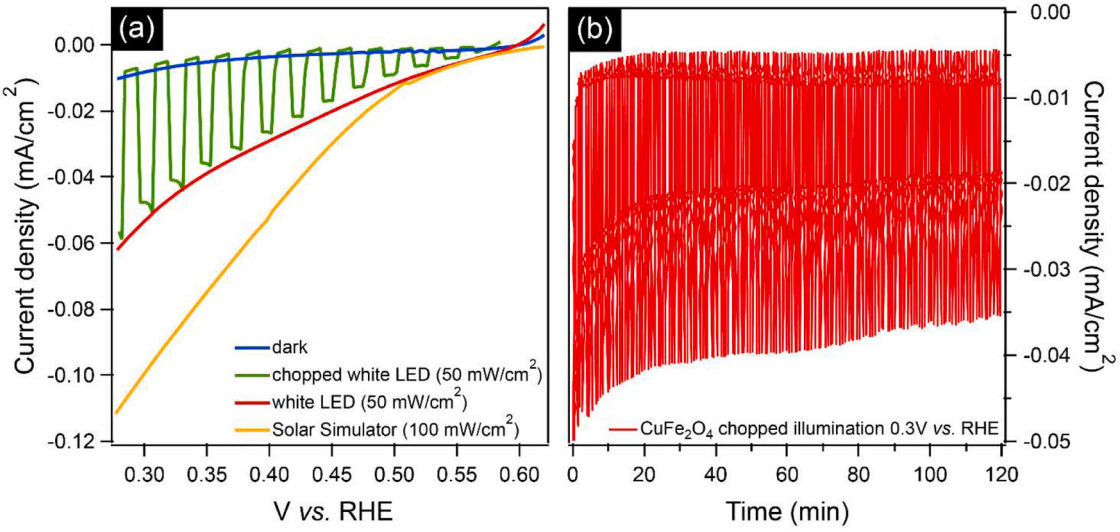

Fig. 7. (a) LSV scans under chopped light, dark, and continuous illumination for $CuFe_2O_4$ in 0.1 M Na_2SO_4 (deaerated with nitrogen). (b) Chopped light chronoamperometry over 2 h at 0.3 V *vs.* RHE.

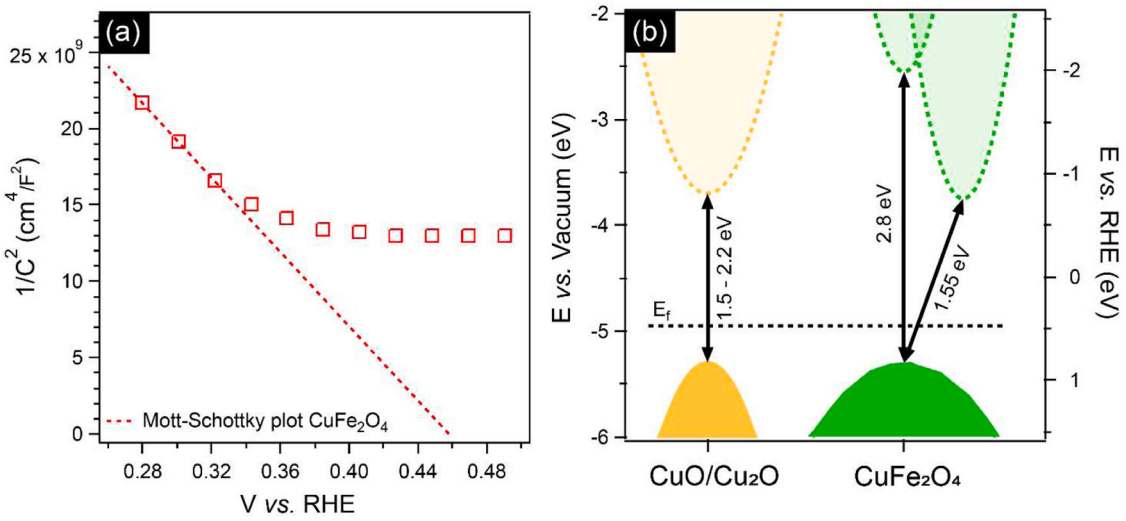

Fig. 8. (a) Mott-Schottky plot for $CuFe_2O_4$ in nitrogen-deaerated 0.1 M Na_2SO_4. (b) Proposed band diagram assuming the occurrence of a thin CuO layer at the surface of $CuFe_2O_4$.

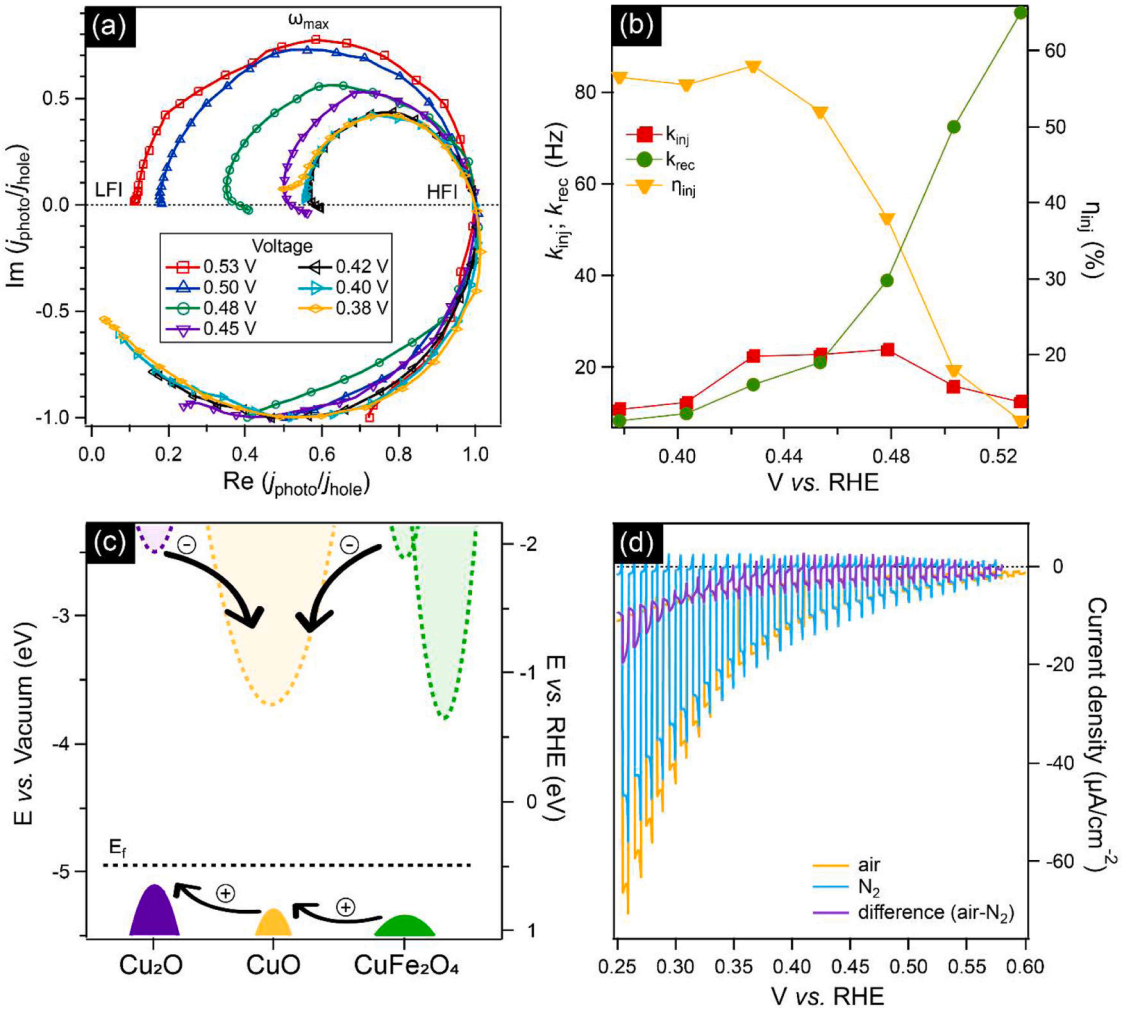

Fig. 9. (a) IMPS Nyquist plots for $CuFe_2O_4$ in 0.1 M Na_2SO_4. (b) k_{inj}, k_{rec}, and charge injection efficiency. (c) Junction scheme showing electron path disruption due to Cu_2O formation. (d) Chopped LSVs in aerated and deaerated Na_2SO_4; the difference curve (purple) shows a phase change at 0.30 V *vs.* RHE.

the presence of an electron scavenger like O_2 enhances the photocurrent, as shown by the difference curve (purple curve) between the aerated (yellow curve) and the deaerated (blue curve) electrolyte solutions in Fig. 9d, confirming electron injection into the electrolyte for O_2

reduction.

Fig. 10 presents the APCE, which quantifies the conversion of absorbed photons into electrical current across wavelengths. The APCE curves (Fig. 10a) show efficiency maxima close to the 0.35 V bias *vs.* RHE with different intensities. A peak efficiency of 0.43 % is obtained at the 405 nm wavelength LED, corresponding to ~3 eV, quite close to the estimated direct band gap of 2.8 eV, thus indicating optimal performance in the lower visible range. A second maximum observed near 550 nm may be attributed to the copper oxides present at the surface. Interestingly, the APCE intensity curve obtained from the 405 nm LED (Fig. 10b, blue curve) starts decreasing below 0.4 V *vs.* RHE, whereas the curve obtained from the 550 nm LED (Fig. 10b, red curve) continues to increase. This behaviour may be rationalized considering a partial reduction of Cu^{2+} to Cu^{+} under cathodic bias on the $CuFe_2O_4$ surface, which suppresses the charge injection into the copper oxides surface and thus decreases the APCE intensity. The third weak APCE maximum visible in the near infrared region (Fig. 10a) is consistent with the fact that the excited electrons, as shown in Fig. 8b, do not acquire enough energy to access the CuO conduction band at the surface. They rather undergo the indirect excitation within the bulk $CuFe_2O_4$, thus resulting in a suppressed contribution to the photocurrent at 700–800 nm.

Overall, the SCBD overcomes many of the limitations associated with the current $CuFe_2O_4$ deposition methods, as the kinetic energy of the clusters and the non-equilibrium nature of the process allow crystallinity control at relatively low substrate temperatures, with the nanogranular structure of the film minimizing the thermal budget for phase evolution, thus obtaining an efficient photoelectrode.

4. Conclusions

A 70±8 nm thin $CuFe_2O_4$ film was successfully deposited on FTO via SCBD for the first time. The photoelectrode is predominantly composed of the tetragonal $CuFe_2O_4$–spinel phase. Although the average Cu:Fe atomic ratio before thermal treatment indicates a slight iron excess, after air annealing at 400 °C, XPS analysis indicates a Cu segregation on the surface due to the formation of a thin CuO/Cu_2O overlayer. This picture is confirmed by STEM-EDX analysis which reveals nanoscale compositional inhomogeneity with local gradients ranging from the expected 1:2 stoichiometry to highly Cu-rich regions (up to 81:1) at the particle surfaces. Interestingly, the formation of tetragonal $CuFe_2O_4$ phase at unusually low temperatures is likely due to the nanogranular nature of the metallic precursor obtained by SCBD.

The electrode exhibits strong visible-light absorption, and very good photocurrent values considering its low thickness and roughness, with a photocurrent onset in Na_2SO_4 electrolyte at 0.6 V *vs.* RHE. The electrode maintains good stability over extended illumination, a behaviour which is also due to the strong adhesion of SCBD films. In addition, its compositional stability is further confirmed by XPS and Raman analyses after PEC work. However, the application of a bias below 0.35 V *vs.* RHE induces the reduction of CuO to Cu_2O at the electrode surface. This effect determines a reduction of the k_{inj} constant as suggested by IMPS analysis, although the charge injection efficiency remains high because of low recombination. This indicates a narrow operational bias window (0.6–0.3 V *vs.* RHE) for stable PEC activity. APCE shows a conversion efficiency peak around 405 nm, consistent with the direct transitions observed from the Tauc plot at 2.8 eV. Furthermore, APCE spectral features support the evolution of interfacial Cu_xO species under bias.

Funding sources

This work was supported by the European Union - Next Generation EU project "Supersonic Cluster beam synthesis of Innovative TRansition metal Oxides PHotoelectrodes for HYdrogen production (SCI-TROPHY)", call MUR PRIN 2022, Prot. 2022474YE8, CUP J53D23007340008, C53D23003710006, as well as by CNR (Progetti di Ricerca @CNR – avviso 2020 - ASSIST) and Padova University (PDiSC#02BIRD2023-UNIPD RIGENERA, DOR 2023–2025) projects.

CRediT authorship contribution statement

Michele Vergari: Writing – review & editing, Writing – original draft, Investigation, Formal analysis, Data curation. **Skerxho Osmani:** Writing – review & editing, Writing – original draft, Investigation, Formal analysis, Data curation. **Ermanno Pierobon:** Writing – review & editing, Writing – original draft, Investigation, Formal analysis, Data curation. **Enrico Scattolin:** Investigation. **Andrea Basagni:** Writing – review & editing, Visualization, Validation, Investigation, Formal analysis. **Alberto Gasparotto:** Writing – review & editing, Visualization, Validation, Investigation, Formal analysis. **Chiara Maurizio:** Writing – review & editing, Visualization, Validation, Investigation, Formal analysis. **Gian Andrea Rizzi:** Writing – original draft, Validation, Supervision, Project administration, Methodology, Investigation, Funding acquisition, Conceptualization. **Luca Gavioli:** Writing – review & editing, Validation, Supervision, Resources, Project administration,

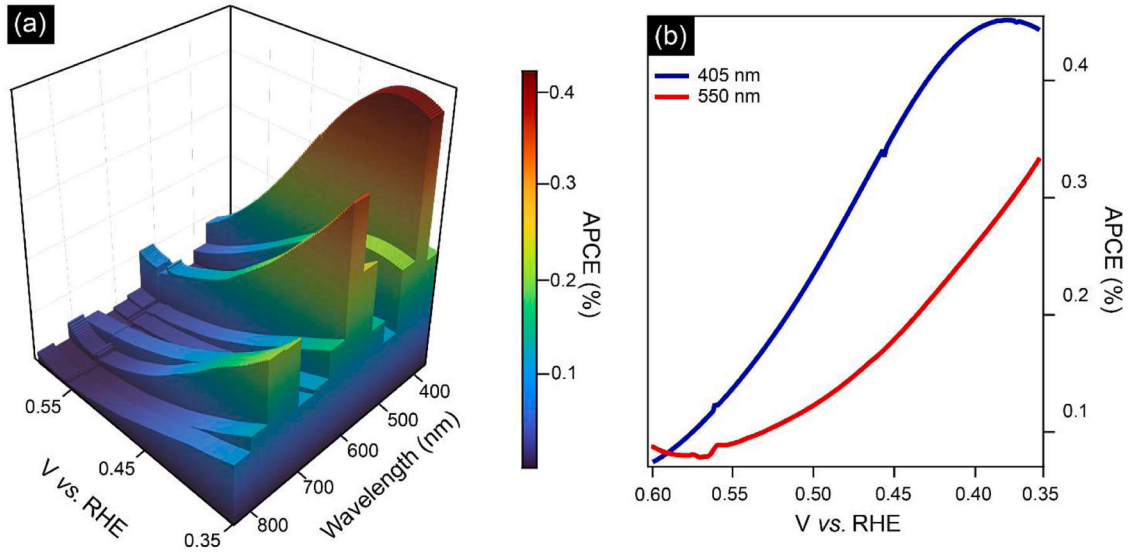

Fig. 10. (a) APCE map for $CuFe_2O_4$ in 0.1 M Na_2SO_4, measured from 0.6 to 0.35 V *vs.* RHE across the 365–810 nm spectral range. (b) APCE intensity at 405 nm (blue spectrum) and 550 nm (red spectrum) in the 0.6 to 0.35 V *vs.* RHE range.

Methodology, Investigation, Funding acquisition, Conceptualization.

Declaration of competing interest

The authors declare that they have no known competing financial interests or personal relationships that could have appeared to influence the work reported in this paper.

Supplementary materials

Supplementary material associated with this article can be found, in the online version, at doi:10.1016/j.apsadv.2026.100999.

Data availability

Data will be made available on request.

References

[1] P. Villars, PAULING FILE in: inorganic solid phases. https://materials.springer.com/isp/crystallographic/docs/sd_1953964, 2022 accessed December 11, 2025.

[2] S. Park, J.H. Baek, L. Zhang, J.M. Lee, K.H. Stone, I.S. Cho, J. Guo, H.S. Jung, X. Zheng, Rapid flame-annealed $CuFe_2O_4$ as efficient photocathode for photoelectrochemical hydrogen production, ACS Sustain. Chem. Eng. 7 (2019) 5867–5874, https://doi.org/10.1021/acssuschemeng.8b05824.

[3] K.M. Rezaul Karim, H.R. Ong, H. Abdullah, A. Yousuf, C.K. Cheng, M.M. Rahman Khan, Photoelectrochemical reduction of carbon dioxide to methanol on p-type $CuFe_2O_4$ under visible light irradiation, Int. J. Hydrog. Energy 43 (2018) 18185–18193, https://doi.org/10.1016/j.ijhydene.2018.07.174.

[4] J. Zander, M. Weiss, R. Marschall, Fast and facile microwave synthesis of cubic $CuFe_2O_4$ nanoparticles for electrochemical CO_2 reduction, Adv. Energy Sustain. Res. 4 (2023) 2200184, https://doi.org/10.1002/aesr.202200184.

[5] L. Cai, J. Guo, T. Liu, J. Tian, Z. Wang, Y. Liu, M.S. Hamdy, X. Sun, Selective photoreduction of nitrate to nitrogen with a two-step process by a KBH_4/Cu(II) modified $CuFe_2O_4$ photocatalyst, Nano Res. 16 (2023) 10462–10475, https://doi.org/10.1007/s12274-023-5696-9.

[6] J. Zander, M.F. Fink, M. Attia, C. Roth, R. Marschall, Selective optimisation of catalytic activity by tuning the structural composition in nanoparticulate $CuFe_2O_4$, Sustain. Energy Fuels 8 (2024) 4848–4863, https://doi.org/10.1039/D4SE00968A.

[7] J.E. Tasca, C.E. Quincoces, A. Lavat, A.M. Alvarez, M.G. González, Preparation and characterization of $CuFe_2O_4$ bulk catalysts, Ceram. Int. 37 (2011) 803–812, https://doi.org/10.1016/j.ceramint.2010.10.023.

[8] V.A. Zhuravlev, R.V. Minin, V.I. Itin, I.Y. Lilenko, Structural parameters and magnetic properties of copper ferrite nanopowders obtained by the sol-gel combustion, J. Alloys Compd. 692 (2017) 705–712, https://doi.org/10.1016/j.jallcom.2016.09.069.

[9] W. Ponhan, S. Maensiri, Fabrication and magnetic properties of electrospun copper ferrite ($CuFe_2O_4$) nanofibers, Solid State Sci. 11 (2009) 479–484, https://doi.org/10.1016/j.solidstatesciences.2008.06.019.

[10] M. Salavati-Niasari, T. Mahmoudi, M. Sabet, S.M. Hosseinpour-Mashkani, F. Soofivand, F. Tavakoli, Synthesis and characterization of copper ferrite nanocrystals via coprecipitation, J. Clust. Sci. 23 (2012) 1003–1010, https://doi.org/10.1007/s10876-012-0486-7.

[11] E.A. Ponomarev, L.M. Peter, A generalized theory of intensity modulated photocurrent spectroscopy (IMPS), J. Electroanal. Chem. 396 (1995) 219–226, https://doi.org/10.1016/0022-0728(95)04115-5.

[12] S. Ravishankar, A. Riquelme, S.K. Sarkar, M. Garcia-Batlle, G. Garcia-Belmonte, J. Bisquert, Intensity-modulated photocurrent spectroscopy and its application to perovskite solar cells, J. Phys. Chem. C 123 (2019) 24995–25014, https://doi.org/10.1021/acs.jpcc.9b07434.

[13] Y. Liu, F. Le Formal, F. Boudoire, L. Yao, K. Sivula, N. Guijarro, Insights into the interfacial carrier behaviour of copper ferrite ($CuFe_2O_4$) photoanodes for solar water oxidation, J. Mater. Chem. A 7 (2019) 1669–1677, https://doi.org/10.1039/C8TA11160J.

[14] M. Einert, A. Waheed, D.C. Moritz, S. Lauterbach, A. Kundmann, S. Daemi, H. Schlaad, F.E. Osterloh, J.P. Hofmann, Mesoporous $CuFe_2O_4$ photoanodes for solar water oxidation: impact of surface morphology on the photoelectrochemical properties**, Chem. – Eur. J. 29 (2023) e202300277, https://doi.org/10.1002/chem.202300277.

[15] S. Osmani, E. Scattolin, M. Vergari, A. Gasparotto, G.A. Rizzi, L. Gavioli, The effect of surface states accumulation on photo-electrochemical performances of $Bi_{24}Fe_2O_{39}$ grown by supersonic beams, J. Phys. Chem. Solids 193 (2024) 112160, https://doi.org/10.1016/j.jpcs.2024.112160.

[16] L. Ciambriello, I. Alessandri, M. Ferroni, L. Gavioli, I. Vassalini, Unexpected resilience of NiFe catalysts for the alkaline oxygen evolution reaction, ACS Appl. Energy Mater. 7 (2024) 3462–3472, https://doi.org/10.1021/acsaem.4c00286.

[17] B.D. Fraters, E. Cavaliere, G. Mul, L. Gavioli, Synthesis of photocatalytic TiO_2 nanocoatings by supersonic cluster beam deposition, J. Alloys Compd. 615 (2014) S467–S471, https://doi.org/10.1016/j.jallcom.2013.12.037.

[18] M. Vergari, S. Osmani, A. Basagni, E. Scattolin, M. Rea, A. Gasparotto, G.A. Rizzi, L. Gavioli, Influence of surface iron content on the photoelectrochemical properties of BiFeO films deposited via SCBD, Mater. Chem. Phys. 337 (2025) 130600, https://doi.org/10.1016/j.matchemphys.2025.130600.

[19] M.I. Díez-García, T. Lana-Villarreal, R. Gómez, Study of copper ferrite as a novel photocathode for water reduction: improving its photoactivity by electrochemical pretreatment, ChemSusChem 9 (2016) 1504–1512, https://doi.org/10.1002/cssc.201600023.

[20] Z. Lin, S. Hao, Z. Li, J. Hu, A. Song, Elucidation of the optical, electronic, and photoelectrochemical properties of p-type $CuFe_2O_4$ photocathodes, Int. J. Hydrog. Energy 77 (2024) 511–519, https://doi.org/10.1016/j.ijhydene.2024.06.248.

[21] A. Herrera-Gomez, M. Bravo-Sanchez, F.S. Aguirre-Tostado, M.O. Vazquez-Lepe, The slope-background for the near-peak regimen of photoemission spectra, J. Electron Spectrosc. Relat. Phenom. 189 (2013) 76–80, https://doi.org/10.1016/j.elspec.2013.07.006.

[22] J.A. Torres-Ochoa, D. Cabrera-German, O. Cortazar-Martinez, M. Bravo-Sanchez, G. Gomez-Sosa, A. Herrera-Gomez, Peak-fitting of Cu 2p photoemission spectra in Cu0, Cu1+, and Cu2+ oxides: a method for discriminating Cu0 from Cu1+, Appl. Surf. Sci. 622 (2023) 156960 https://doi.org/10.1016/j.apsusc.2023.156960.

[23] M.C. Biesinger, Advanced analysis of copper X-ray photoelectron spectra, Surf. Interface Anal. 49 (2017) 1325–1334, https://doi.org/10.1002/sia.6239.

[24] J.I. Pankove, Optical Processes in Semiconductors, Dover Publications, Inc, New York, 2012.

[25] A.R. Zanatta, Revisiting the optical bandgap of semiconductors and the proposal of a unified methodology to its determination, Sci. Rep. 9 (2019) 11225, https://doi.org/10.1038/s41598-019-47670-y.

[26] B. Klahr, S. Gimenez, F. Fabregat-Santiago, T. Hamann, J. Bisquert, Water oxidation at hematite photoelectrodes: the role of surface states, J. Am. Chem. Soc. 134 (2012) 4294–4302, https://doi.org/10.1021/ja210755h.

[27] A. Hankin, F.E. Bedoya-Lora, J.C. Alexander, A. Regoutz, G.H. Kelsall, Flat band potential determination: avoiding the pitfalls, J. Mater. Chem. A 7 (2019) 26162–26176, https://doi.org/10.1039/C9TA09569A.

[28] Z. Chen, H.N. Dinh, E. Miller, Photoelectrochemical Water Splitting: Standards, Experimental Methods, and Protocols, Springer New York, New York, NY, 2013, https://doi.org/10.1007/978-1-4614-8298-7.

[29] C. Jiang, S.J.A. Moniz, A. Wang, T. Zhang, J. Tang, Photoelectrochemical devices for solar water splitting – materials and challenges, Chem. Soc. Rev. 46 (2017) 4645–4660, https://doi.org/10.1039/C6CS00306K.

[30] A. Podestà, F. Borghi, M. Indrieri, S. Bovio, C. Piazzoni, P. Milani, Nanomanufacturing of titania interfaces with controlled structural and functional properties by supersonic cluster beam deposition, J. Appl. Phys. 118 (2015) 234309, https://doi.org/10.1063/1.4937549.

[31] M. Bottagisio, V. Balzano, L. Ciambriello, L. Rosa, G. Talò, A.B. Lovati, E. De Vecchi, L. Gavioli, Exploring multielement nanogranular coatings to forestall implant-related infections, Front. Cell. Infect. Microbiol. 13 (2023), https://doi.org/10.3389/fcimb.2023.1128822.

[32] V. Balzano, E. Cavaliere, M. Fanetti, S. Gardonio, L. Gavioli, The role of substrate on thermal evolution of Ag/TiO2 nanogranular thin films, Nanomaterials 11 (2021) 2253, https://doi.org/10.3390/nano11092253.

[33] I.N. Kholmanov, E. Barborini, S. Vinati, P. Piseri, A. Podestà, C. Ducati, C. Lenardi, P. Milani, The influence of the precursor clusters on the structural and morphological evolution of nanostructured TiO_2 under thermal annealing, Nanotechnology 14 (2003) 1168–1173, https://doi.org/10.1088/0957-4484/14/11/002.

[34] A. Subha, M.G. Shalini, B. Sahu, S.C. Sahoo, Structural transformation and magnetic properties of copper ferrite nanoparticles prepared by sol–gel method, J. Mater. Sci. Mater. Electron. 29 (2018) 20790–20799, https://doi.org/10.1007/s10854-018-0221-8.

[35] M.D.P. Silva, F.C. Silva, F.S.M. Sinfrônio, A.R. Paschoal, E.N. Silva, C.W. A. Paschoal, The effect of cobalt substitution in crystal structure and vibrational modes of $CuFe_2O_4$ powders obtained by polymeric precursor method, J. Alloys Compd. 584 (2014) 573–580, https://doi.org/10.1016/j.jallcom.2013.08.074.

[36] P.J. Pinhero, J.W. Anderegg, D.J. Sordelet, M.F. Besser, P.A. Thiel, Surface oxidation of Al-Cu-Fe alloys: a comparison of quasicrystalline and crystalline phases, Philos. Mag. B 79 (1999) 91–110, https://doi.org/10.1080/13642819908206784.

[37] J. Morales, J.P. Espinos, A. Caballero, A.R. Gonzalez-Elipe, J.A. Mejias, XPS study of interface and ligand effects in supported Cu_2 O and CuO nanometric particles, J. Phys. Chem. B 109 (2005) 7758–7765, https://doi.org/10.1021/jp0453055.

[38] D. Tahir, S. Tougaard, Electronic and optical properties of Cu, CuO and Cu_2 O studied by electron spectroscopy, J. Phys. Condens. Matter 24 (2012) 175002, https://doi.org/10.1088/0953-8984/24/17/175002.

[39] V.R. Galakhov, A.I. Poteryaev, E.Z. Kurmaev, V.I. Anisimov, S. Bartkowski, M. Neumann, Z.W. Lu, B.M. Klein, T.-R. Zhao, Valence-band spectra and electronic structure of $CuFeO_2$, Phys. Rev. B 56 (1997) 4584–4591, https://doi.org/10.1103/PhysRevB.56.4584.

[40] P.S. Bagus, C.J. Nelin, C.R. Brundle, B.V. Crist, N. Lahiri, K.M. Rosso, Combined multiplet theory and experiment for the Fe 2p and 3p XPS of FeO and Fe2O3, J. Chem. Phys. 154 (2021) 094709, https://doi.org/10.1063/5.0039765.

[41] T.-C. Lin, G. Seshadri, J.A. Kelber, A consistent method for quantitative XPS peak analysis of thin oxide films on clean polycrystalline iron surfaces, Appl. Surf. Sci. 119 (1997) 83–92, https://doi.org/10.1016/S0169-4332(97)00167-0.

[42] K. Cui, M. Sun, T. Gong, J. Xu, L. Hou, C. Yuan, Band gap and oxygen vacancy engineering of honeycomb-like $CuFe_2O_4$ spinels toward enhanced high infrared emissivity, J. Am. Ceram. Soc. 106 (2023) 4233–4245, https://doi.org/10.1111/jace.19067.

[43] J. Zander, F. Daumann, R. Loukrakpam, C. Roth, B. Weber, R. Marschall, Correlations of calcination temperature with the catalytic properties of $CuFe_2O_4$ for the synthesis of green fuels, Adv. Energy Sustain. Res. 6 (2025) 2400281, https://doi.org/10.1002/aesr.202400281.
[44] P. Makuła, M. Pacia, W. Macyk, How to correctly determine the band gap energy of modified semiconductor photocatalysts based on UV–Vis spectra, J. Phys. Chem. Lett. 9 (2018) 6814–6817, https://doi.org/10.1021/acs.jpclett.8b02892.
[45] Y. Hermans, A. Klein, H.P. Sarker, M.N. Huda, H. Junge, T. Toupance, W. Jaegermann, Pinning of the fermi level in $CuFeO_2$ by polaron formation limiting the photovoltage for photochemical water splitting, Adv. Funct. Mater. 30 (2020) 1910432, https://doi.org/10.1002/adfm.201910432.
[46] S. Maitra, S. Pal, T. Maitra, S. Halder, S. Roy, Solvothermal etching-assisted phase and morphology tailoring in highly porous $CuFe_2O_4$ nanoflake photocathodes for solar water splitting, Energy Fuels 35 (2021) 14087–14100, https://doi.org/10.1021/acs.energyfuels.1c02090.
[47] L. Trinh, K. Bienkowski, P. Wróbel, M. Pisarek, A. Parzuch, N. Nawaz, R. Solarska, New concept for the facile fabrication of core–shell CuO@$CuFe_2O_4$ photocathodes for PEC application, Materials 15 (2022) 1029, https://doi.org/10.3390/ma15031029.
[48] Q. Wang, Y. Wang, Re-examination of CuO reduction steps and understanding of the factors influencing the cyclic voltammetry profile of CuO, J. Electrochem. Soc. 165 (2018) A2439–A2445, https://doi.org/10.1149/2.0161811jes.
[49] Z. Lin, S. Hao, G. Liu, D. Xu, X. Liu, J. Hu, A. Song, *In situ* construction of $CuFe_2O_4$/CuO heterojunction photocathode for improved solar water splitting, J. Alloys Compd. 1042 (2025) 184174, https://doi.org/10.1016/j.jallcom.2025.184174.
[50] Y. Yang, D. Xu, Q. Wu, P. Diao, Cu_2O/CuO bilayered composite as a high-efficiency photocathode for photoelectrochemical hydrogen evolution reaction, Sci. Rep. 6 (2016) 35158, https://doi.org/10.1038/srep35158.
[51] L. Girardi, G.A. Rizzi, L. Bigiani, D. Barreca, C. Maccato, C. Marega, G. Granozzi, Copper vanadate nanobelts as anodes for photoelectrochemical water splitting: influence of CoO_x overlayers on functional performances, ACS Appl. Mater. Interfaces 12 (2020) 31448–31458, https://doi.org/10.1021/acsami.0c06915.